PAPER

Check for updates

A combination of proton spin diffusion NMR and molecular simulations to probe supramolecular assemblies of organic molecules in nanoporous materials†

Eddy Dib, [ID] *[a] Beatriz Bernardo-Maestro,[b] Fernando López-Arbeloa,[c] Joaquín Pérez-Pariente [ID] [b] and Luis Gómez-Hortigüela [ID] *[b]

In this work we show the use of high-resolution ^{1}H MAS NMR to distinguish between two kinds of aggregation states of (1*R*,2*S*)-ephedrine, a chiral organic structure directing agent, occluded within AFI-type microporous aluminophosphates. We investigate in particular the supramolecular assembly of the molecules through π···π type interactions of their aromatic rings when confined within the one-dimensional AFI channels. A series of high-resolution two-dimensional spin diffusion spectra combined with molecular simulations and DFT calculations allowed us to distinguish different aggregation states of ephedrine molecules and precisely estimate the distances between the aromatic rings and their closest protons inside the zeolite channels as a consequence of distinct proton spin diffusion profiles.

1. Introduction

The development of chiral solid materials able to perform chemical operations in adsorption or catalysis in an enantioselective way is crucial in the chemical industry (especially in the pharmaceutical sector) in order to produce pure enantiomers of chiral compounds.[1] Among the different types of active solids, zeolites, which are microporous crystalline materials based on connected SiO_4 tetrahedra, have been proposed as excellent candidates for producing chiral-active solid materials as they can potentially combine their unique shape-selectivity capabilities with enantioselective properties.[2–4]

The most straightforward strategy to induce chirality in zeolite frameworks is through the use of chiral organic molecules as structure-directing agents (SDA).[5,6] These SDAs organize the inorganic units around in a particular geometry,

driving the crystallization pathway towards a particular framework type, remaining occluded within the porous structure after the crystallization process. Therefore, the study at molecular level of the structure-directing effect of chiral organic molecules during the synthesis of zeolite microporous materials is fundamental in order to realize a transfer of chirality from organic species to inorganic zeolite frameworks.[7] This has been recently accomplished for the STW chiral framework by using computationally-designed chiral SDAs that follow the helicoidal pattern of the micropores of the STW network.[8,9]

In an attempt to induce chirality in zeolite frameworks, we proposed the use of the alkaloid (1*R*,2)-ephedrine (EPH) as chiral SDA (Scheme 1).[10] In previous works we showed that these molecules tend to form supramolecular aggregates when confined within the one-dimensional pores of the AFI aluminophosphate framework, in which part of the aluminum atoms of the framework have been isomorphically substituted by Mg^{2+} cations.[11,12] Indeed, the aggregation of these species

[a]*Normandie Univ, ENSICAEN, UNICAEN, CNRS, Laboratoire Catalyse et Spectrochimie, 14000 Caen, France. E-mail: eddy.dib@ensicaen.fr*
[b]*Instituto de Catálisis y Petroleoquímica, ICP-CSIC. C/Marie Curie 2, 28049 Madrid, Spain. E-mail: lhortiguela@icp.csic.es*
[c]*Departamento de Química Física, Universidad del País Vasco, Apartado 644, 48080 Bilbao, Spain*

†Electronic supplementary information (ESI) available: Fig. S1, XRD patterns, Fig. S2, diffuse reflectance UV-VIS spectra, Fig. S3, thermogravimetric analyses, Fig. S4, SEM images, Fig. S5, solid state ^{13}C MAS NMR spectra, Fig. S6, solid state ^{27}Al MAS NMR spectra, Fig. S7, solid state ^{31}P MAS NMR spectra, Fig. S8, liquid ^{1}H NMR, Fig. S9, measured peak intensities as a function of spin diffusion mixing time. See DOI: 10.1039/d2dt00497f
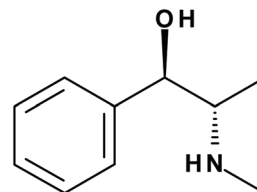
Scheme 1 Molecular structure of (1*R*,2*S*)-ephedrine.

confined within AFI nanopores (7.3 Å of diameter) can be altered by modifying the crystallization conditions, in particular with gel composition and crystallization temperature:[13] high Mg and low SDA contents and low crystallization temperatures favor the incorporation of EPH as monomers (Fig. 1-top), whilst the opposite (low Mg, high SDA and high crystallization temperature) favor the occlusion of EPH as dimers (Fig. 1-bottom). Moreover, the molecular structure of the ephedrine derivative also strongly affects the supramolecular behaviour, with (1*R*,2*S*)-ephedrine displaying the strongest self-assembly trend.[11,14,15]

As a matter of fact, the development of supramolecular assemblies of organic species as structure-directing entities has become a fundamental concept in zeolite synthesis that has led to the crystallization of a number of open frameworks or new compositions of already known structures.[16–25] Under this strategy, which has been referred as supramolecular assembly templating (SAT), simple organic species form supramolecular aggregates, usually through development of π–π type interactions (provided aromatic rings are present), whose larger size tends to drive the crystallization pathway towards large-pore and/or large-cavity-based materials. In this context, the monitoring of the supramolecular behavior of these molecules confined within microporous materials represents a crucial issue. As shown in previous works, UV-VIS fluorescence spectroscopy has proved as an efficient tool to monitor the aggregation state of the molecules confined in nanoporous spaces.[17,26] The formation of supramolecular dimers through stacking of the aromatic rings involves strong π–π type interactions that result in a reorganization of the electronic levels, causing a red-shift of the emission band of the aromatic ring.

Solid-state nuclear magnetic resonance (NMR) is a powerful tool to probe non-covalent host–guest interactions in supramolecular assemblies, *e.g.* hydrogen bonding, van der Waals and π–π interactions, giving unique, atomic-level information about structure and dynamics of guest molecules adsorbed in solid materials.[27,28] However, getting precise information about internuclear distances when proton nuclei are involved is hindered by intense dipole–dipole couplings, giving rise to spectral broadenings.[29] Highly resolved spectra are usually obtained using magic angle spinning that aims to average dipole–dipole couplings among other anisotropic interactions. Hence, the increase of resolution is on detriment of precious information like internuclear distances. For this reason, several two-dimensional recoupling techniques have been designed to reintroduce the dipole–dipole coupling in one dimension while having a highly resolved spectrum in the other. These techniques are either homonuclear or heteronuclear.[30] We have recently localized silanol defects in as-synthesized silicalite-1 using homonuclear ^{1}H–^{1}H DQ-SQ recoupling technique,[31] and probed the aluminum distribution in ZSM-5 using heteronuclear ^{29}Si–^{27}Al symmetry-based recoupling technique.[32] Moreover, proton spin diffusion (PSD) process describes the magnetization exchange between protons driven by the dipolar coupling dependent on internuclear distances, potentially giving access to information about internuclear distances.[33]

In this work we use high-resolution ^{1}H NMR measurement of PSD process combined with DFT calculations, to distinguish different supramolecular behaviors of ephedrine molecules when confined within nanopores, getting a precise idea on the intermolecular distances separating the molecules, providing precious information about packing interactions in host–guest systems.

2. Experimental

2.1 Synthesis and general characterization

Synthesis of MgAPO-5 materials using (1*R*,2*S*)-ephedrine (EPH) as SDA was carried out following our previously reported recipes.[13] The solids were characterized by powder X-ray diffraction (XRD) (Philips X'PERT diffractometer with Cu [Kα] radiation with a Ni filter), thermogravimetric analyses (TGA) (Perkin-Elmer TGA7 instrument [heating rate = 20 °C min^{-1}] under air flow), and UV–Visible diffuse reflectance spectroscopy (UV-Vis Cary 5000 Varian spectrophotometer). Solid state UV-visible fluorescence emission spectra were recorded in a RF-5300 Shimadzu fluorimeter in the front-face configuration.

2.2 Nuclear magnetic resonance

Magic-angle spinning (MAS) NMR spectra were acquired at a 11.7 T Bruker Avance III-HD spectrometer, using 1.9 OD-mm probe head for ^{1}H. The rotor was spun with a spinning rate of
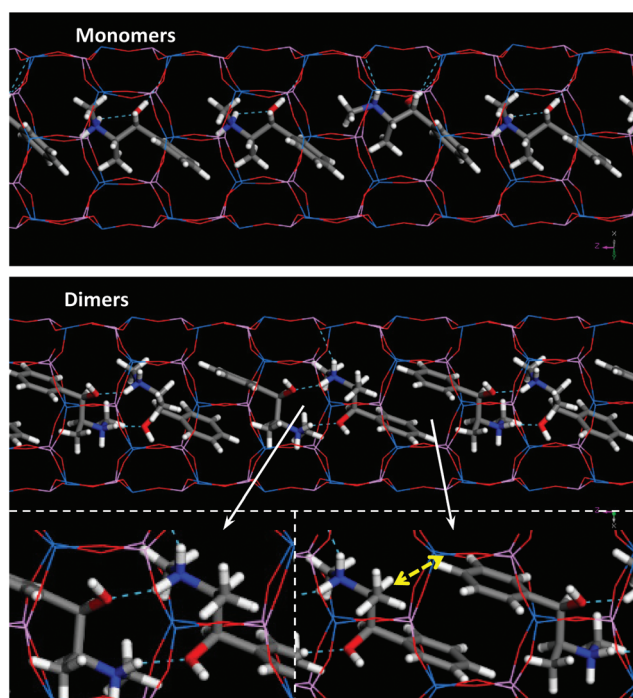

Fig. 1 Location of ephedrine molecules in monomer (top) or dimer (bottom) configurations. Yellow arrow indicates short H(*para*)⋯H3 intermolecular distances (see text below).

40 kHz, a radiofrequency power of 125 kHz was used, and 16 scans were acquired with a recycle delay of 5 seconds. The experimental parameters used for other nuclei are given in the ESI.† The ^{1}H–^{1}H spin diffusion spectra were acquired with short spin diffusion mixing times varying from 0 to 1 millisecond.

2.3 Computational details

Plane waves DFT-D theoretical calculations have been performed with the CASTEP module in Material Studio,[34] using PBE[35] as functional; the Grimme dispersion term[36] was used to account for dispersion interactions. The most stable location of ephedrine in different configurations in the AFI systems, with 3 [for monomers] or 4 [for dimers] protonated EPH cations in 1 × 1 × 3 AFI supercells in the required orientations, was found by molecular mechanics-based simulated annealing calculations, using the cvff forcefield.[37] The systems were then geometry optimized at DFT-D level. Calculation of the NMR chemical shifts were performed with the gauge-including projector augmented-wave method (GIPAW) developed by Pickard and Mauri.[38] ^{1}H chemical shieldings (σ) were converted into chemical shifts (δ) by using reference values of σ_{ref} = 30, in order to make them roughly coincide with the expected chemical shift values of the aromatic protons ($\tilde{\delta} = \sigma_{ref} - \sigma$); averaged values for the different chemically equivalent protons in the different molecules present in the models will be considered.

3. Results and discussion

In previous works we showed that EPH tends to direct the crystallization of the AFI framework structure, which is based on one-dimensional 12-MR channels (Fig. 1). Interestingly, we had observed that the supramolecular behavior of this molecule when confined within nanoporous materials can be altered by tuning the synthesis conditions.[13] In this work, two MgAPO-5 (AFI-framework type) samples have been studied for which the synthesis conditions were adjusted in order to have different aggregation states of ephedrine molecules, arranged as monomers (M) or dimers (D) (Fig. 1). X-ray diffraction patterns showed that both samples are pure MgAPO-5 materials (Fig. S1†).

Depending on the crystallization temperature and the gel composition, two different EPH species in the AFI channels can be spectroscopically identified. The UV-VIS fluorescence spectrum of the sample obtained at 165 °C from gel composition 0.32 MgO : 1 EPH : 0.84 Al$_2$O$_3$: 1 P$_2$O$_5$: 100 H$_2$O (with high Mg and water contents) consists in an emission peak centered at 282 nm with an overlapped vibrational shoulder at around 295 nm (Fig. 2-blue) which is assigned to the EPH monomer. In contrast, the fluorescence spectrum of the sample obtained upon a reduction of the Mg and water contents (gel composition of 1 EPH : 0.22 MgO : 0.89 Al$_2$O$_3$: 1 P$_2$O$_5$: 50 H$_2$O) and an increase in the crystallization temperature (to 180 °C) presents a main broad emission band in the
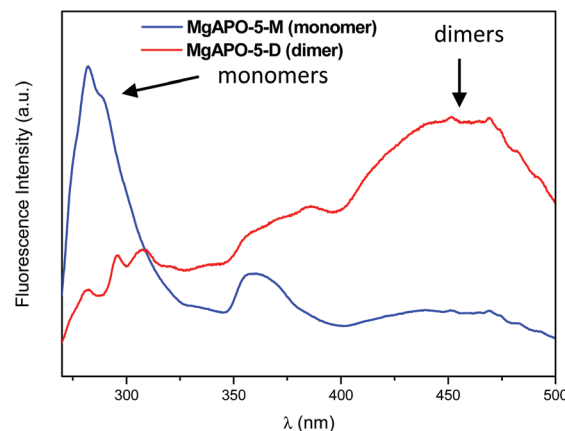

Fig. 2 Fluorescence spectra of MgAPO-5-M (blue line) and MgAPO-5-D (red line).

blue VIS region between 425 and 500 nm (Fig. 2-red) attributed to an aggregate (dimer) state of EPH[26] (no higher-order aggregates can be confined within the AFI channels); in this case, $\pi\cdots\pi$ interactions between stacked aromatic rings composing the dimer involve a reorganization of the electronic levels, promoting a stabilization of the π^* molecular orbital which reduces the transition energy, resulting in such shift to higher wavelengths. The formation of monomer and dimer species of EPH in the AFI channels is confirmed by UV/VIS diffuse reflectance spectroscopy (Fig. S2†), with two clear absorption peaks at ~215 and ~260 nm (with a vibrational profile) for EPH monomers (Fig. S2†-blue for MgAPO-5-M) and a broad and an additional overlapping absorption band centered at around 360 nm, characteristic of the presence of EPH dimers (Fig. S2†-red for MgAPO-5-D).

Interestingly, TGA results (Fig. S3†) show a higher incorporation of organics in the sample where dimers predominate (MgAPO-5-D, with 1.26 EPH per u.c., compared to MgAPO-5-M, with 1.13 EPH per u.c.). This suggests a more efficient packing of ephedrine molecules in the AFI channels when they arrange as dimers (see Fig. 1). In the MgAPO-5-M sample, the lower organic incorporation is accompanied by a slightly higher water content. SEM images (Fig. S4†) show the occurrence of hexagonal prismatic crystals typical of AFI materials, these crystals being larger in sample MgAPO-5-D, obtained from more concentrated gels. Moreover, SEM also shows the presence of a minor amount of amorphous material in the MgAPO-5-M sample.

^{13}C MAS NMR (Fig. S5†) shows all the typical bands associated to EPH, evidencing the resistance of ephedrine molecules to the hydrothermal treatment and their integral incorporation in both MgAPO-5 materials; broader bands are observed for dimers in MgAPO-5 (Fig. S5,† red line). ^{27}Al MAS NMR spectra (Fig. S6†) show a band at 38 ppm characteristic of tetrahedral aluminum in the AFI framework; a minor presence of penta-coordinated Al at 8 ppm is also observed, more abundant in sample MgAPO-5-M, possibly coming from the amorphous material, as observed by SEM (see Fig. S4†). ^{31}P MAS NMR

(Fig. S7†) shows two bands at −30 and −24 ppm, characteristic of P(4Al) and P(1Mg,3Al) environments in the AFI tetrahedral network, respectively,[39] confirming the incorporation of Mg atoms in the AFI framework. This incorporation is higher for sample MgAPO-5-D than for MgAPO-5-M (1.30 and 1.03 Mg per u.c., respectively, as obtained from deconvolution of the ^{31}P NMR spectra), despite the higher concentration of Mg in the synthesis gel used for MgAPO-5-M. Indeed, these Mg contents are in line with the EPH contents (as calculated from TGA) since these (protonated) molecules provide charge-balance for the isomorphic substitution of Al^{3+} by Mg^{2+}. The lower packing efficiency of ephedrine monomers (limited to 1.0–1.1 EPH per u.c.) in this material thus restricts the incorporation of Mg in the framework to 1.1.

The conventional ^{1}H MAS NMR spectra of the as-synthesized MgAPO-5 materials are shown in Fig. 3. They display a number of resonances between 1 and 8 ppm assigned to ephedrine protons. Four clear NMR signals are observed for EPH monomers at 0.9, 2.1, 3.1 and 4.9 ppm (blue line), which are assigned to protons 1, 2, 3 and 4, respectively, apart from a broad band at 7.3 ppm with several peaks corresponding to aromatic protons. When we compare with the dimer spectrum, several clues reveal the existence of different molecular assemblies in both samples. The first observation is the increase of the peaks' width in the spectrum of sample MgAPO-5-D, where the observed loss of resolution may be due to (i) the aggregation of the molecules (wider distribution of chemical environments giving rise to wider chemical shift ranges for each proton in the molecule) or (ii) the dipolar coupling between the protons (directly related to the inter-nuclear distances). Indeed, several overlapped peaks in the H2–H3 region are observed, which might be associated to dimers in different orientations. In addition, a notable difference is observed on dimers where a new band arises at 6.7 ppm as a shoulder of the aromatic band, which must be associated to π···π stacked aggregates.

In an attempt to understand these differences, we used DFT calculations to predict the chemical shifts as a function of the supramolecular state (Table 1). We focus on aromatic protons

Fig. 3 ^{1}H NMR spectra of samples MgAPO-5-M (bottom, blue line) and MgAPO-5-D (top, red line).

Table 1 DFT calculated chemical shifts for EPH cations in different supramolecular aggregation states

	H *meta*	H *ortho*	H *para*	CHOH (4)	CHCH₃ (3)	CH₃N (2)	CHCH₃ (1)
M	7.6	7.5	7.4	5.1	2.6	1.5	0.5
D	7.0	7.1	6.5	5.0	3.0	2.9	1.4

which are the ones that will mostly feel the π···π stacking interaction upon formation of supramolecular dimers and the ones less affected by the free-movement of protons (considering that these are static DFT calculations); indeed, differences in H2 and H1 predicted shifts (Table 1) might be associated to static DFT calculations artifacts and the presence of different molecular conformations/orientations. Theoretical results show that protons that mostly feel the π···π stacking interaction are those in *meta* and especially in *para* positions since they are closer to the aromatic ring of the other molecule composing the dimer (see Fig. 1), explaining that these protons show a larger difference in the predicted chemical shift upon aggregation. Interestingly, our modeling results predict a clear shift of the band corresponding to H in *para* position of the aromatic rings upon formation of dimers towards lower chemical shifts (from 7.4 to 6.5 ppm, Table 1), which must be due to the proximity to the next EPH molecule in the dimer. This observation might explain the shoulder observed in the ^{1}H NMR spectrum of MgAPO-5-D sample.

Two-dimensional (2D) spin diffusion ^{1}H MAS NMR allows to get precious information on the internuclear distances from the measurements of the proton spin diffusion (PSD) coefficients.[40,41] They are directly related to the internuclear distances when short diffusion periods are used, as relaxation effects can be ignored for short spin diffusion times.[42,43] However, the spin diffusion rate depends also on the orientation of the internuclear vector in the solid and the MAS rate, and a phenomenological multi-spin kinetic rate matrix approach was proposed. Thus, the combination of PSD approach with DFT calculations allows an accurate determination of [1]H–[1]H distances.[44]

Fig. 4 shows two examples of 2D PSD spectra recorded with a mixing time of 0 and 1 milliseconds. The intensity of the peaks varies with the mixing time t_{SD} due to proton spin diffusion; the evolution of the polarization P_{ij} obeys the equation $P_{ij}(t_{SD}) = \exp[-k_{ij} \cdot t_{SD}]_{ij} M_z^0$, with k_{ij} being the spin diffusion rate constant between a pair of spins i and j, and M_z^0 the longitudinal magnetization. Then, with increasing spin diffusion time, the intensity of diagonal cross peaks decreases while off-diagonal cross peaks get more intense, as shown in Fig. S9.† Interestingly, the spin diffusion rate varies from one proton to another but interference may occur between several types of intermolecular and intramolecular protons, and it is complex to estimate all distances between all protons, especially inside the channels where a statistical distribution of negative and positive charges occurs with possibly different configurations. Then, we will only consider protons of the
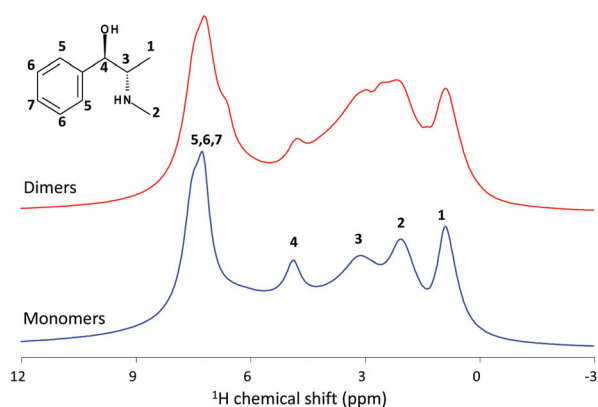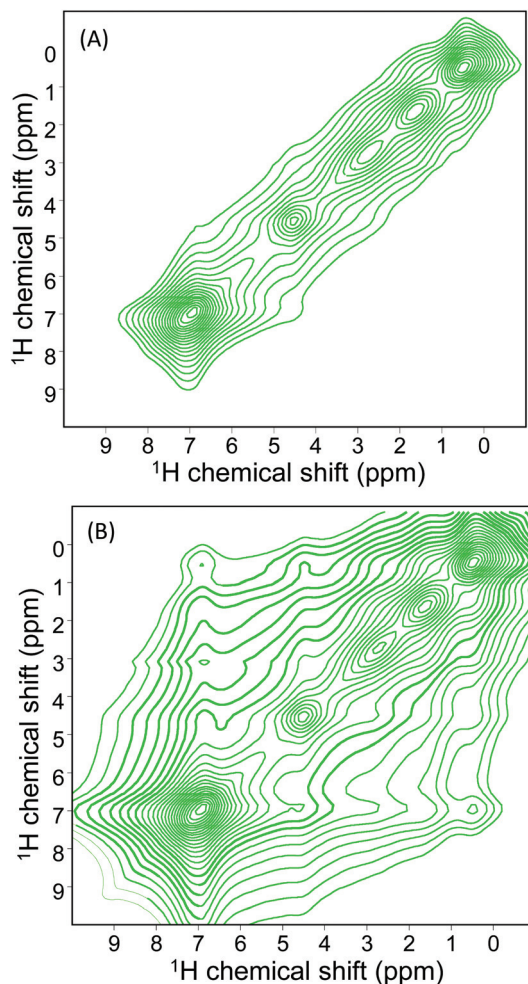
Fig. 4 ^{1}H NMR spin diffusion spectrum of the sample MgAPO-5-M (monomers) recorded at 500 MHz at two different mixing times 0.0 (A) and 1.0 ms (B).
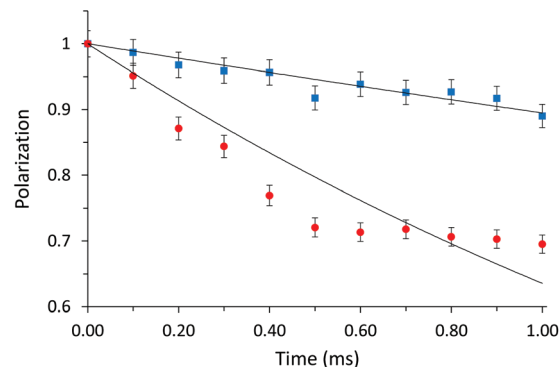

Fig. 5 Evolution of the diagonal peak in spin diffusion experiments corresponding to the phenyl group in the samples MgAPO-5-M (blue squares) and MgAPO-5-D (red dots), and the corresponding fits (black lines) using the diffusion equation.

phenyl groups, the ones most involved in the π···π stacking interactions. It is also important to note that all relaxation processes are neglected at this time-scale and proton–proton spin-diffusion processes are the only ones responsible for the decay or build-up of the diagonal or off-diagonal peaks, respectively.

Fig. 5 shows the evolution of the diagonal peak area corresponding to the phenyl groups with spin diffusion time for MgAPO-5-M and -D samples. The spin diffusion rate constant k_{ij} is much higher for sample with EPH dimers: 1.1134 ± 0.0636 ms^{-1} for MgAPO-5-M $vs.$ 4.6841 ± 0.3249 ms^{-1} for MgAPO-5-D; the high error for the latter indicates the eventual presence of some monomers. These differences are mainly driven by dipolar couplings, spin diffusion processes, occurring either between equivalent or different spins, which depend directly on internuclear distances and, as a consequence, on supramolecular assemblies. They are described using the diffusion equation (*vide supra*).

Nevertheless, the spin diffusion rate is directly related to ^{1}H–^{1}H distances *via* the equation $k_{ij} = A(\mu_0\gamma_H^2 h/8\pi)^2/r_{ij}^6$, where

μ_0, γ_H, and h are physical constants, r_{ij} is the internuclear distance between atoms i and j, and A is a phenomenological scaling factor, set to 10^{16} for both normalized curves. Using this equation, we can estimate average distances separating aromatic rings from their closest protons in both samples, considering the diffusion with the first neighbor spin as the most effective one. These distances correspond to 3.27 and 4.15 Å for MgAPO-5-D and MgAPO-5-M, respectively, being lower for the arrangement of dimers. This proves the higher packing efficiency of EPH when arranged as dimers, which prompts a higher incorporation of organics, as observed from TGA and indirectly also by ^{31}P NMR results. The incorporation of dimers is a consequence of π···π interactions between the aromatic rings, but can also be assisted by the potential development of intermolecular H-bonds between consecutive dimers to compensate for the electrostatic repulsion generated by their positive charge associated to N.

In order to correlate such packing efficiency and the associated higher proton spin diffusion rate with shorter interatomic distances between protons, we ran molecular dynamics simulations (100 ps in the NVT ensemble at 25 °C) for monomers and dimers occluded within AFI channels, and calculated the interatomic distance between protons as the radial distribution function between selected groups of H atoms (Fig. 6). Overall, results show a stronger intermolecular interaction (shorter intermolecular distances) between all protons when they arranged as dimers (Fig. 6A), given by the higher RDF intensity of dimers between 2 and 7 Å (red line). This involves a higher packing efficiency for dimers, as previously observed. Such shorter inter-proton distances for dimers is a consequence of the interaction between aromatic protons composing the dimer (Fig. 6B, red line), as evidenced by the RDF peak between 3 and 6 Å, which is not present when they arrange as monomers (Fig. 6B, blue line). In addition, if we focus on the intermolecular distances between aromatic and the rest of protons (Fig. 6C), we observe a strong H···H intermolecular interaction between 2 and 3 Å for dimers which is absent in monomers; this short dimer distance corresponds to the dis-

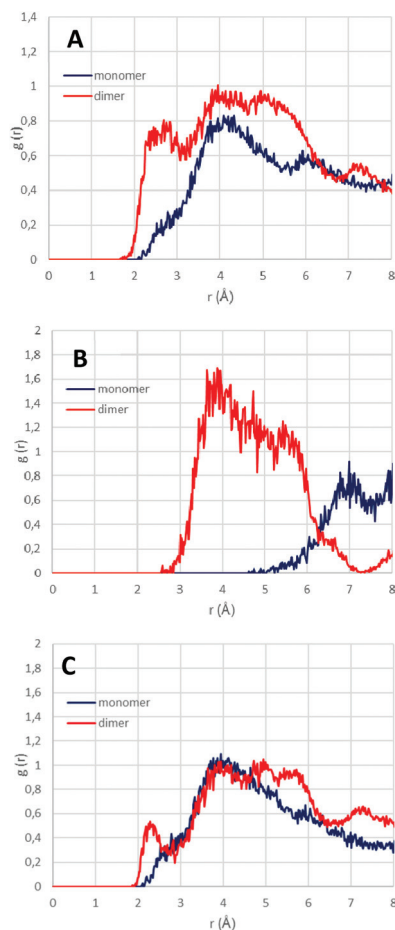**Dalton Transactions**

Paper

Fig. 6 Intermolecular RDF between protons during MD simulations for monomers (blue lines) and dimers (red lines): A: RDF between all EPH protons (top); B: RDF between aromatic protons (middle); C: RDF between aromatic and non-aromatic protons (bottom). All RDF calculations exclude intramolecular interactions.

tance between aromatic protons in *para* position and H3 (from CH-CH₃ group) (see Fig. 1-bottom, yellow dashed arrow). These results are a direct consequence of the high packing efficiency when EPH form supramolecular aggregates. Indeed, if we look at the overall intermolecular H···H distances (Fig. 6A), a short distance between 2 and 3 Å is found for dimers, while this short distance shifts to ~4 Å for monomers, which are in good agreement with the distances found by our proton spin diffusion model, explaining the higher ^{1}H spin diffusion rates for EPH aggregates.

4. Conclusions

In this work, we used high-resolution proton spin diffusion MAS NMR combined with DFT calculations to analyse the supramolecular state of organic structure-directing agents confined within the nanopores of microporous materials, which is a direct consequence of the distinct packing efficiency of the guest species as a function of their aggregation state. A series

of two-dimensional spin diffusion spectra allowed us to estimate the distances and interactions between the aromatic rings and their first proton neighbours inside the nanopores. This methodology may be very useful to understand the incorporation of organic species in host–guest nanoporous systems, providing important information on how efficiently guest species pack upon confinement.

Author contributions

BBM performed the synthesis and general characterization of the materials; ED performed the NMR study; FLA did the fluorescence spectroscopy study, JPP supervised the work, LGH conceptualized and supervised the work, and did the computational work. All authors wrote and revised the manuscript.

Conflicts of interest

There are no conflicts to declare.

Acknowledgements

Notes and references

1 K. Harris and S. J. Thomas, *ChemCatChem*, 2009, **1**, 223–231.
2 M. E. Davis, *Top. Catal.*, 2003, **25**, 3–7.
3 J. Yu and R. Xu, *J. Mater. Chem.*, 2008, **18**, 4021–4030.
4 M. E. Davis, *ACS Catal.*, 2018, **8**, 10082–10088.
5 L. Gómez-Hortigüela and M. A. Camblor, Introduction to the zeolite structure-directing phenomenon by organic species: general aspects, in *Insights into the chemistry of organic structure-directing agents in the synthesis of zeolitic materials. Struc. Bond*, ed. L. Gómez-Hortigüela, Springer, Cham, 2017, vol. 175.
6 M. Moliner, F. Rey and A. Corma, *Angew. Chem., Int. Ed.*, 2013, **52**, 13880–13889.
7 L. Gómez-Hortigüela and B. Bernardo-Maestro, Chiral organic structure-directing agents, in *Insights into the chem-*

istry of organic structure-directing agents in the synthesis of zeolitic materials. Struc. Bond, ed. L. Gómez-Hortigüela, Springer, Cham, 2017, vol. 175.

8 S. K. Brand, J. E. Schmidt, M. W. Deem, F. Daeyaert, Y. Ma, O. Terasaki, M. Orazov and M. E. Davis, *Proc. Natl. Acad. Sci. U. S. A.*, 2017, **114**, 5101–5106.

9 J. H. Kang, L. B. McCusker, M. W. Deem, C. Baerlocher and M. E. Davis, *Chem. Mater.*, 2021, **33**, 1752–1759.

10 T. Álvaro-Muñoz, F. López-Arbeloa, J. Pérez-Pariente and L. Gómez-Hortigüela, *J. Phys. Chem. C*, 2014, **118**, 3069–3077.

11 B. Bernardo-Maestro, F. López-Arbeloa, J. Pérez-Pariente and L. Gómez-Hortigüela, *J. Phys. Chem. C*, 2015, **119**, 28214–28225.

12 B. Bernardo-Maestro, F. López-Arbeloa, J. Pérez-Pariente and L. Gómez-Hortigüela, *Microporous Mesoporous Mater.*, 2017, **254**, 211–224.

13 B. Bernardo-Maestro, M. D. Roca-Moreno, F. López-Arbeloa, J. Pérez-Pariente and L. Gómez-Hortigüela, *Catal. Today*, 2016, **277**, 9–20.

14 B. Bernardo-Maestro, P. Gálvez, D. González, F. López-Arbeloa, J. Pérez-Pariente and L. Gómez-Hortigüela, *J. Phys. Chem. C*, 2018, **122**, 20377–20390.

15 B. Bernardo-Maestro, E. Vos, F. López-Arbeloa, J. Pérez-Pariente and L. Gómez-Hortigüela, *Microporous Mesoporous Mater.*, 2017, **239**, 432–443.

16 C. Paris and M. Moliner, Role of Supramolecular Chemistry During Templating Phenomenon in Zeolite Synthesis, in *Insights into the chemistry of organic structure-directing agents in the synthesis of zeolitic materials. Structure and Bonding*, ed. L. Gómez-Hortigüela, Springer, Cham, 2017, vol. 175.

17 A. Corma, F. Rey, J. Rius, M. J. Sabater and S. Valencia, *Nature*, 2004, **431**, 287–290.

18 M. Moliner, *Top. Catal.*, 2015, **58**, 502–512.

19 F. J. Chen, Y. Xu and H. B. Du, *Angew. Chem., Int. Ed.*, 2014, **53**, 9592–9596.

20 Z. H. Gao, F. J. Chen, L. Xu, L. Sun, Y. Xu and H. B. Du, *Chem. – Eur. J.*, 2016, **22**, 14367–14372.

21 D. R. Liu, Z. H. Gao, W. W. Zi, J. Zhang, H. B. Du and F. J. Chen, *Microporous Mesoporous Mater.*, 2019, **276**, 232–238.

22 R. Martínez-Franco, A. Cantín, M. Moliner and A. Corma, *Chem. Mater.*, 2014, **26**, 4346–4353.

23 R. Martínez-Franco, A. Cantín, A. Vidal-Moya, M. Moliner and A. Corma, *Chem. Mater.*, 2015, **27**, 2981–2989.

24 F. J. Chen, Z. H. Gao, L. L. Liang, J. Zhang and H. B. Du, *CrystEngComm*, 2016, **18**, 2735–2741.

25 W.-W. Zi, Z. Gao, J. Zhang, J.-H. Lv, B.-X. Zhao, Y.-F. Jiang, H.-B. Du and F.-J. Chen, *Microporous Mesoporous Mater.*, 2019, **290**, 109654.

26 L. Gómez-Hortigüela, F. López-Arbeloa, F. Corà and J. Pérez-Pariente, *J. Am. Chem. Soc.*, 2008, **130**, 13274–13284.

27 S. P. Brown, I. Schnell, J. D. Brand, K. Mullen and H. W. Spiess, *J. Am. Chem. Soc.*, 1999, **121**, 6712–6718.

28 A. R. Hughes and F. Blanc, *CrystEngComm*, 2021, **23**, 2491–2503.

29 S. P. Brown, *Solid State Nucl. Magn. Reson.*, 2012, **41**, 1–27.

30 M. H. Levitt, *Encycl. Nucl. Magn. Reson.*, 2007, **9**, 165–196.

31 E. Dib, J. Grand, S. Mintova and C. Fernandez, *Chem. Mater.*, 2015, **27**, 7577–7579.

32 E. Dib, T. Mineva, E. Veron, V. Sarou-Kanian, F. Fayon and B. Alonso, *J. Phys. Chem. Lett.*, 2018, **9**, 19–24.

33 J. Li, S. Li, A. Zheng, X. Liu, N. Yu and F. Deng, *J. Phys. Chem. C*, 2017, **121**, 14261–14268.

34 S. Clark, M. Segall, C. Pickard, P. Hasnip, M. Probert, K. Refson and M. Payne, *Z. Kristallogr.*, 2005, **220**, 567–570.

35 J. P. Perdew, K. Burke and M. Ernzerhof, *Phys. Rev. Lett.*, 1996, **77**, 3865–3868.

36 S. Grimme, *J. Comput. Chem.*, 2004, **25**, 1463–1473.

37 P. Dauber-Osguthorpe, V. A. Roberts, D. J. Osguthorpe, J. Wolff, M. Genest and A. T. Hagler, *Proteins: Struct., Funct., Genet.*, 1988, **4**, 31–47.

38 C. J. Pickard and F. Mauri, *Phys. Rev. B: Condens. Matter Mater. Phys.*, 2001, **63**, 245101.

39 M. da S. Machado, J. Pérez-Pariente, E. Sastre, D. Cardoso, M. V. Giotto, J. L. García-Fierro and V. Fornés, *J. Catal.*, 2002, **205**, 299–308.

40 B. Elena, G. Pintacuda, N. Mifsud and l. Emsley, *J. Am. Chem. Soc.*, 2006, **128**, 9555–9560.

41 C. J. Pickard, E. Salager, G. Pintacuda, B. Elena and L. Emsley, *J. Am. Chem. Soc.*, 2007, **129**, 8932–8933.

42 E. Salager, R. S. Stein, C. J. Pickard, B. Elena and L. Emsley, *Phys. Chem. Chem. Phys.*, 2009, **11**, 2610–2621.

43 E. Salager, G. M. Day, R. S. Stein, C. J. Pickard, B. Elena and L. Emsley, *J. Am. Chem. Soc.*, 2010, **132**, 2564–2566.

44 C. Martineau, J. Senker and F. Taulelle, *Annu. Rep. NMR Spectrosc.*, 2014, **82**, 1–57.